# Time-Series and Extended Karhunen–Loève Analysis of Turbulent Drag Reduction in Polymer Solutions

**Sung-Ning Wang and Michael D. Graham**
Dept. of Chemical and Biological Engineering, University of Wisconsin-Madison, Madison, WI 53706

**Friedemann J. Hahn**
Graduate School of Excellence advanced Manufacturing Engineering, Universität Stuttgart, Nobelstr. 12, 70569
Stuttgart, Germany

**Li Xi**
Dept. of Chemical Engineering, McMaster University, Hamilton, ON L8S 4L8, Canada

*DOI 10.1002/aic.14328*

*Direct numerical simulations and statistical analysis techniques are used to study the drag-reducing effect of polymer additives on turbulent channel flow in minimal domains. Additionally, a new formulation of Karhunen–Loève decomposition for viscoelastic flows is introduced, allowing the dominant features of the polymer stress fields to be characterized. In minimal channels, there are intervals of "active" and "hibernating" turbulence that display very different structural and energetic characteristics; the present work illustrates how the statistics of these intervals evolve over the entire range of drag reduction (DR) levels. The effect of viscoelasticity on minimal channel turbulence is twofold: first, it strongly suppresses the active turbulent dynamics that predominate in Newtonian flow and second, at sufficiently high Weissenberg number it stabilizes the dynamics of hibernating turbulence, allowing it to predominate in the maximum drag reduction regime. In this regime, the stress fluctuations become delocalized from the wall region, encompassing the entire flow domain.* © 2014 American Institute of Chemical Engineers *AIChE J*, 60: 1460–1475, 2014
*Keywords: turbulence, fluid mechanics, complex fluids*

## Introduction

Addition of flexible long-chain polymer molecules to liquids at very low concentrations can lead to substantial reductions of turbulent friction drag.[1–3] In addition to its obvious applications in fluid transport systems, it has also attracted much attention for its fundamental theoretical significance. Study of this problem might contribute not only to the knowledge of flow-polymer interactions, but also to advancements in the understanding of turbulent flows. In particular, with a thorough understanding of the mechanism by which polymer causes high amounts of drag reduction (DR), rational flow control schemes achieving comparable levels of energy savings without adding polymer can be envisioned.

The most intriguing qualitative observation associated with DR is the so-called maximum drag reduction (MDR) asymptote, an upper bound on the level of DR that can be achieved channel or pipe flow of a drag-reducing fluid.[1,4] This asymptotic limit is universal in the sense that it is insensitive to changes in the polymer solution (concentration, molecular weight, or even polymer type): for a given Reynolds number Re, the maximum amount of DR achievable with polymer is invariant. Although MDR is sometimes regarded as a high Reynolds number phenomenon, it is not, having been is observed at Reynolds numbers all the way down to the point of transition to turbulence.[1,5] Conversely, it is a *high Weissenberg number* phenomenon, where the Weissenberg number *Wi* is the product of a polymer relaxation time $\lambda$ and a characteristic strain rate in the flow.

Bulk flow data obtained from DR experiments in channel or tube flow are often shown in Prandtl–von Kármán coordinates, that is, a plot of average velocity $U^+_{\text{avg}} \equiv U_{\text{avg}}/u_\tau$ vs. friction Reynolds number $\text{Re}_\tau \equiv \rho u_\tau l/\eta$. Here, $\rho$ is the fluid density, $\eta$ is the total viscosity, and $l$ is a characteristic length scale of the flow geometry; the friction velocity $u_\tau \equiv \sqrt{\tau_{\text{w}}/\rho}$ is a characteristic velocity scale for near-wall turbulence, where $\tau_{\text{w}}$ is the mean wall shear stress; the superscript "+" denotes quantities nondimensionalized with inner scales, that is, velocities scaled by $u_\tau$ and lengths scaled by $\eta/\rho u_\tau$. A schematic Prandtl–von Kármán plot for Newtonian and polymeric flow is shown in Figure 1.

A primary distinguishing feature of MDR is its mean velocity profile $U_m(y)$, where $y$ is distance from the wall. In the MDR regime, a universal log-law relationship $U^+_m(y^+) \approx 11.7\, y^+ - 17.0$ is observed across most of the geometry, regardless of the flow rate and polymer solution used. Additionally, many studies have reported significantly reduced, sometimes even vanishing, magnitudes of the Reynolds shear stress as

---

Correspondence concerning this article should be addressed to M. Graham at graham@engr.wisc.edu.

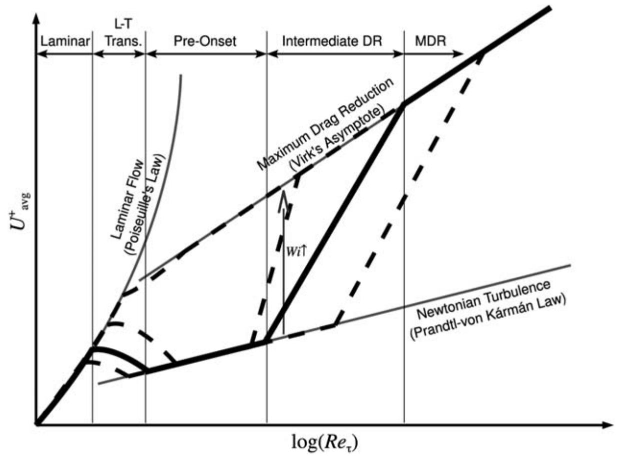

**Figure 1. Schematic Prandtl–von Kármán plot.**

**Thin vertical lines mark the transition points on a typical experimental path shown as a thick solid line. Other dashed lines represent different experimental paths that represent, for example, changes in polymer molecular weight or channel size.**

MDR is approached.[6–9] Flow visualization has revealed flow structures near MDR that are distinctively different than those of Newtonian turbulence.[9–13] Streamwise vortices, which dominate Newtonian near-wall dynamics, are significantly weakened at MDR. Low-speed streaks, which in the Newtonian case show sinuous and patchy shapes along the flow direction, become smooth and elongated, and their streamwise waviness is substantially weakened.

Any successful theory of MDR should be able to consistently answer two questions. First, what sustains turbulence at MDR? Polymer reduces drag by weakening normal turbulent motions (as further discussed later)—it is unknown why this effect saturates. Second, why is MDR universal with respect to polymer-related properties? It is very counterintuitive that polymer-related properties do not affect the turbulent dynamics (or at least its mean flow statistics) once this asymptote is reached.

Many theoretical attempts to address these issues have been made. An early approach is the "elastic sublayer" model proposed by Virk.[1,4] In this model, DR only occurs in the buffer layer ($y^+ \approx 5-30$ for Newtonian flow) of near-wall turbulence: viscoelasticity changes $U_m(y)$ in this layer to follow the MDR log-law (thus termed the "elastic sublayer"); beyond the buffer layer, turbulence is assumed to be unaffected by polymer and $U_m(y)$ returns to the same slope as the von Kármán log-law for Newtonian turbulence, only with a larger intercept. With increasing viscoelasticity and DR, the buffer layer thickness grows and thus, shifts the crossover point away from the wall. MDR is reached when the buffer layer fills the entire flow geometry.

Aside from the phenomenological rather than mechanistic nature of this model, evidence contradictory to it has emerged. A number of experimental and computational studies show that $U_m(y)$ within the buffer layer does not follow the Virk-MDR log-law in the intermediate DR regime, but instead lies between the profiles of Newtonian turbulence and MDR.[6–9,14,15] In addition, several studies[6–9] have found that the von Kármán log-law is observed only in cases with low degrees of DR (LDR), whereas in cases with high degrees of DR (HDR), but before MDR is reached, a log-law slope higher than the von Kármán slope is observed across most part of the channel. In addition to this change between local (in the buffer layer) and global (across the flow geometry) increase of the $U_m(y)$ profile slope, qualitative changes are observed in other flow statistics during this LDR-HDR transition. These findings indicate that many aspects of the mechanism of convergence of viscoelastic turbulence to MDR are missing from this model.

In another approach that combines ideas of polymer elasticity theory and scaling arguments about the scales of turbulent structures, Sreenivasan and White[16] predicted that MDR occurs when polymer effects are felt at the largest scale of the flow: that is, the size of the flow geometry. This theory is very similar to that of Virk discussed above in that the MDR limit is set by the geometric length scale of the flow. Again limited by the extent of available experimental data, this model is far from providing a complete physical picture of MDR.

Another recent approach is based on phenomenological ansatzes regarding Reynolds shear stresses and eddy viscosities.[17–21] In particular, Benzi and coworkers[17,18] combine these ideas with the observation that in some experiments (e.g., Ref. 6) the Reynolds shear stress nearly vanishes to develop a model in which there is a limit to the log-law slope that can be achieved before the turbulent state loses existence and the flow relaminarizes—the authors identify this limiting slope with the MDR asymptote. Conversely, many studies have observed nonzero Reynolds shear stress in regimes where the Virk MDR profile was also observed[7–9]; additionally, the mechanism that sustains turbulence at MDR is not addressed by the model. Finally, results presented by Xi and Graham[22] and below show that a log-law slope that approaches the Virk value can be observed as a recurrent transient in Newtonian flows, where the Reynolds stresses are finite and polymer stresses nonexistent.

These models have contributed interesting insights into this problem, but none seem to be capable of completely answering the two primary questions raised above. In addition, evidence against each major model of MDR has been reported.[3] It is not surprising though to find significant gaps in these approaches, given that all of them are based on a very limited volume of experimental data. The limitations of existing experimental research are especially reflected in the lack of data on the spatiotemporal intermittency in flow structures in drag-reduced flow, and recent work indicates that this intermittency may hold the key to understanding the full mechanism of MDR.

Some important information on this topic has been obtained by direct numerical simulation (DNS) of turbulent flow of polymer solutions using relatively simple continuum models of the polymer dynamics. Most DNS studies (see, e.g., Refs. 9,23–25) have been performed in settings as close to the experimental conditions as possible, that is, large simulation boxes and $Re$ as high as computationally accessible (yet at present still significantly lower than many experiments). In contrast, the present work is also built around DNS results, but in small "minimal" domains in which the dynamics, although still complex, are simpler in that the small domain does not permit large numbers of interacting dynamical structures to arise. This "minimal flow unit" (MFU) approach has shed substantial light on Newtonian turbulence,[26–28] and the aim of the present work as well as recent past work by the present authors[15,22,29,30] is to extend the approach to the understanding of DR and specifically MDR.

For Newtonian flow, the seminal study of Jiménez and Moin[26] showed that all important quantities in the MFU display large fluctuations in an intermittent cyclic fashion. Specifically, they described dynamics in which the wall shear stress as well as the fluctuations rapidly increase or "bloom" during the "active" part of the cycle. Hamilton et al.[27] and Jiménez and Pinelli[28] further describe this cycle. They note that during time intervals in which the wall shear stress is near its lowest values, very little streamwise variation is seen in the flow—there is one nearly straight streak, which eventually develops streamwise waviness and "breaks down" into highly three-dimensional (3-D) turbulence. Eventually, the flow again becomes dominated by a single nearly streamwise streak and the cycle repeats.

One data analysis approach that has been useful in characterizing turbulent flows is the so-called Karhunen–Loève (KL) decomposition, often called Proper Orthogonal Decomposition in the fluid dynamics literature. This methodology was introduced in the context of turbulent flows by Lumley and coworkers[31,32] and consists of determining a set of time-independent flow fields—KL modes—that on average capture the most kinetic energy of the turbulent flow. This approach and a new generalization that we propose for viscoelastic flows are described in detail below. For channel flows, the dominant structures are so-called "roll modes" consisting of pairs of counter-rotating streamwise-invariant vortices in the near-wall region[33,34]. The next most energetic modes have streamwise dependence and are sometimes called propagating modes. In combination with the roll modes these capture the basic structure of the near-wall quasistreamwise vortices. Webber et al.[34] performed KL decomposition of simulations in a minimal channel, describing a small number of what they called "entropy events," in which there is first a peak in the instantaneous energy of the roll modes and subsequently a peak in the energy of the most energetic 3-D modes. Based on this structural description, these results are clearly consistent with those of Refs. 26–28. In the nomenclature of the present work, intervals (infrequent in the Newtonian case) that are dominated by nearly streamwise-invariant structures will be denoted as "hibernating," while the highly 3-D phases will be called "active." We shall be particularly interested in the structure and statistics of these phases, and especially how they are affected by viscoelasticity.

De Angelis et al.[35] pioneered the application of KL analysis to viscoelastic turbulence. Their study focused on one parameter set at relatively low Weissenberg number, examining the distribution of fluctuating kinetic energy among the KL modes. The results showed that at the Weissenberg number studied, viscoelasticity only redistributes the kinetic energy of the dominant modes without changing the modes themselves. The dominant modes in viscoelastic flow were found to contain a much higher fraction of the total energy than those in Newtonian flow, at the expense of the modes with finer-scale structure. These findings were confirmed and extended by Beris and coworkers,[12,36] who performed KL analysis on viscoelastic cases with medium and high degree of DR, respectively. They show that as viscoelasticity increases, the same amount of kinetic energy are distributed in much fewer modes, that is, the dimension of the flow is significantly reduced. These studies established the first picture of KL analysis on viscoelastic turbulent flows. However, their discussions are mostly confined to the energy spectra without detailed examination of eigenmode structures. One limitation of these and other previous applications of the KL analysis to viscoelastic flows is that the usual KL analysis only considers the velocity field—information about the polymer stress field is not included in the analysis and the resulting KL modes describe only velocity, not stress. We address this limitation below.

The MFU results described above illustrate qualitatively the nature of the intermittency observed in near-wall turbulence. An increase in intermittency is very commonly noted as an aspect of turbulent DR[14,25,37–39] and is understood qualitatively to reflect the spatiotemporal changes in the near-wall coherent structures. (Changes in intermittency with viscoelasticity are also observed in homogeneous turbulence.[40–43]) In terms of quantitative measures of intermittency, however, results are very sparse. The most relevant work in this regard seems to be that of Beris and coworkers,[38,39] who illustrated the changes due to viscoelasticity in time correlations of KL modes and probability distribution functions of velocity fluctuations for turbulent channel flow. Furthermore, the connections between observed changes in intermittency and changes in flow structure are unknown.

Some recent progress has been made, however, by careful examination of a large number of viscoelastic MFU solutions covering a wide range of polymer-related parameters in the plane Poiseuille geometry.[15,22,29,30] Perhaps the most interesting result from this approach was identification of the connection between hibernating turbulence, which as noted above is a feature of Newtonian minimal channel flows, and MDR.[22,30] In all transient MFU trajectories studied (both viscoelastic and Newtonian), intervals with weak turbulence intensity and significantly lower-than-average wall shear stress were observed. These intervals typically last for a few hundred time units (TU; defined by the convection time scale $l/U$, where $l$ is a geometric length scale and $U$ is a bulk-flow velocity scale, or $\approx 5l/u_\tau$ ($l/u_\tau$ is the eddy turnover time), before the stronger "active" turbulence reappears.

Even in the Newtonian limit, flow structures within hibernation intervals are strikingly similar to MDR, a fact that had not previously been pointed out. Instantaneous mean velocity profiles in these intervals are drastically different from those during active turbulence, and in particular can reach the same slope as that of the Virk MDR asymptote. In addition, flow structures of hibernating turbulence display significantly weaker streamwise vortices, as well as streamwise streaks that barely vary at all along the streamwise direction; both of these features are observed in experiments near MDR. Further evidence of the transient presence of MDR-like dynamics in Newtonian flow is the recent work of Dubief et al.,[44] who observed in a simulation of Newtonian boundary layer flow that at a spatial position just upstream of where vortices and turbulence spots form, the mean velocity profile looks strikingly similar to the Virk MDR profile.

The overall picture that arises from these MFU studies is the following: in Newtonian turbulence, the flow stays active for the majority of the time and only enters hibernation on rare occasions. Active intervals are dominated by strong 3-D, coherent vortical motions. Once $Wi$ exceeds an onset value $Wi_{\mathrm{onset}} \approx 10$, these flow structures start to transiently stretch the polymer chains. This polymer stretching leads to a weakening of the coherent structures, leading to reduction of the friction drag[37,45–50]; this effect is widely regarded as the primary mechanism operating at low levels of DR.[3] As $Wi$ further increases, there is a further transition, at $Wi=Wi_c$ ($\approx 18$ under the conditions studied), beyond which the active turbulence persistently stretches the polymer chains—during an active interval they are deformed more rapidly than they can relax, so their stress accumulates over time and finally reaches a threshold value beyond which the active turbulence can no longer sustain itself. The flow then enters hibernation and stays there for a time interval during which the drag is low and the polymer molecules relax in the weak hibernating flow field. Eventually this interval ends, the turbulence becomes active again and the cycle repeats in a stochastic manner. This cycle is illustrated in Figure 2. Higher values of log-law slope represent hibernating states with lower friction drag, that is, higher DR. Therefore, the anticorrelation between the instantaneous levels of polymer stretching and DR is clearly seen here. A related anticorrelation has been observed in the spatial development of viscoelastic boundary layer turbulence.[51,52]

These studies were limited to moderate Weissenberg number, a restriction that is surmounted in the present work by determining (approximate) minimal channel sizes at high Weissenberg number: we show here the statistics of active and hibernating intervals over a range of $Wi$ from Newtonian to MDR. Furthermore, an extended version of the KL decomposition is presented that allows direct incorporation of stress field information in the analysis. This analysis is then combined with a simple conditional sampling approach that allows the behavior in active and hibernating intervals to be studied separately. Integration of MFU studies, the framework of active and hibernating turbulence and the extended KL decomposition allow substantial progress in developing a unified framework for understanding DR from onset to the MDR asymptote.

## Model Formulation and Simulation Methodology

We consider flow driven by a constant mean pressure gradient in the plane Poiseuille geometry. The $x$, $y$, and $z$ coordinates are aligned with the streamwise, wall-normal, and spanwise directions, respectively. Here, the half channel height $l$ of the channel is used as the characteristic length scale; the velocity scale is the Newtonian laminar centerline velocity $U$ at the given pressure drop. Because the pressure drop is fixed, the overall momentum balance requires that the time-averaged wall shear rate is exactly 2 based on the zero-shear viscosity. Note that the flow exhibits shear thinning behavior due to the particular polymer model [finitely extensible nonlinear elastic (FENE-P)] considered here. In consequence, the time-averaged wall shear rate is slightly greater than 2 by less than 3% according to the viscosity ratio parameter used in the simulations. The no-slip boundary condition is applied at the walls $y=\pm 1$, and periodic boundary conditions are adopted in the $x$ and $z$ directions; the periods in these directions are denoted $L_x$ and $L_z$. The conservation equations of momentum and mass are

$$\frac{\partial \boldsymbol{v}}{\partial t}+\boldsymbol{v}\cdot\nabla\boldsymbol{v}=-\nabla p+\frac{\beta}{\mathrm{Re}}\nabla^2\boldsymbol{v}+\frac{2(1-\beta)}{\mathrm{ReWi}}\frac{b+5}{b}\left(\nabla\cdot\boldsymbol{\tau}_{\mathrm{p}}\right) \qquad (1)$$

$$\nabla\cdot\boldsymbol{v}=0 \qquad (2)$$

Time $t$ is scaled with $l/U$ and pressure $p$ with $\rho U^2$. Correspondingly, $\mathrm{Re}\equiv\rho Ul/(\eta_{\mathrm{s}}+\eta_{\mathrm{p}})$ ($\rho$ is the total density of the

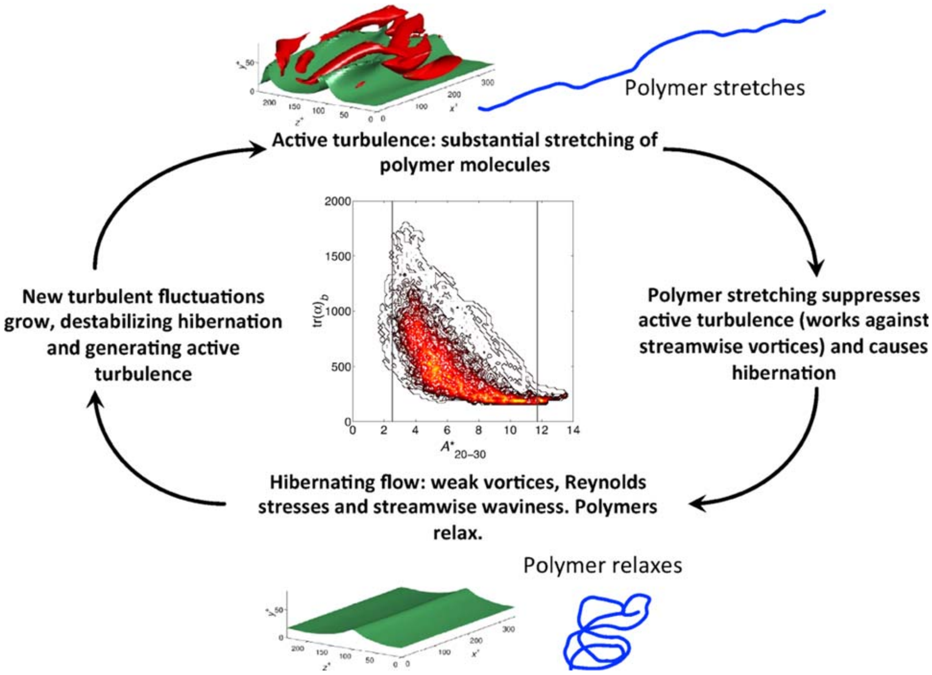

**Figure 2. Schematic of the stochastic cycle displayed by viscoelastic turbulent channel flow in a MFU at low Reynolds number ($\approx 3000$) and moderate Weissenberg number ($\approx 25$).**

**The plot in the center is the joint probability distribution function of spatially averaged polymer stretch tr $\alpha$ and instantaneous log-law slope $A^*$. The asterisk denotes quantities nondimensionalized with inner units based on the instantaneous area-averaged wall shear stress rather than the time- and area-averaged value. The isosurface plots show streamwise velocity (green) and vortex strength (red) at active and hibernating instants in the bottom half of the channel. This figure is composed from results in Ref. 30. [Color figure can be viewed in the online issue, which is available at wileyonlinelibrary.com.]**

fluid; $(\eta_s+\eta_p)$ is the total zero-shear rate viscosity; hereinafter, subscript "s" represents "solvent," that is, the Newtonian contribution, and subscript "p" represents the polymer contribution) and $Wi \equiv 2\lambda U/l$, which is the product of the polymer relaxation time $\lambda$ and the mean wall shear rate. Under this definition, the friction Reynolds $\mathrm{Re}_\tau \equiv \rho u_\tau l/(\eta_s+\eta_p)=\sqrt{2\mathrm{Re}}$ and the eddy turnover time $l/u_\tau=\sqrt{\mathrm{Re}/2}$. The viscosity ratio $\beta \equiv \eta_s/(\eta_s+\eta_p)$ is the ratio of the solvent viscosity and the total zero-shear viscosity. For dilute polymer solutions, $1-\beta$ is proportional to the polymer concentration. The last term on the right-hand side of Eq. 1 captures the polymer effects on the flow field, where the polymer stress tensor $\boldsymbol{\tau}_p$ is modeled by the FENE-P constitutive equation[53]

$$\frac{\boldsymbol{\alpha}}{1-\frac{\mathrm{tr}\,(\boldsymbol{\alpha})}{b}}+\frac{Wi}{2}\left(\frac{\partial\boldsymbol{\alpha}}{\partial t}+\boldsymbol{v}\cdot\boldsymbol{\nabla}\alpha-\boldsymbol{\alpha}\cdot\boldsymbol{\nabla}\boldsymbol{v}-(\boldsymbol{\alpha}\cdot\boldsymbol{\nabla}\boldsymbol{v})^{\mathrm{T}}\right)=\left(\frac{b}{b+2}\right)\boldsymbol{\delta} \tag{3}$$

$$\boldsymbol{\tau}_p=\left(\frac{\boldsymbol{\alpha}}{1-\frac{\mathrm{tr}\,(\boldsymbol{\alpha})}{b}}-\left(1-\frac{2}{b+2}\right)\boldsymbol{\delta}\right) \tag{4}$$

In Eqs. 3 and 4, polymer molecules are modeled as FENE dumbbells: two beads connected by a FENE spring. The variable $\boldsymbol{\alpha}$ is the nondimensional polymer conformation tensor $\boldsymbol{\alpha} \equiv \langle \boldsymbol{qq} \rangle$, where $\boldsymbol{q}$ is a nondimensional end-to-end vector of the dumbbells. The parameter $b$ defines the maximum extensibility of the dumbbells; $\max\,(\mathrm{tr}\,(\boldsymbol{\alpha})) < b$. The importance of $\beta$ and $b$ becomes apparent in considering the extensibility parameter $Ex$, defined as the polymer contribution to the steady-state stress in uniaxial extensional flow, in the high $Wi$ limit. For the FENE-P model, $Ex=2b(1-\beta)/3\beta$. For a dilute solution $(1-\beta \ll 1)$, significant effects of polymer on turbulence are only expected when $\mathrm{Ex} \gg 1$. Simulations in this study are all performed at $\mathrm{Re}=3600(\mathrm{Re}_\tau=84.85)$; for the viscoelastic cases, $\beta=0.97$ and $b=1\cdot 10^4$ are used, which gives $Ex=206.19$.

The whole equation system is coupled and advanced in time with a third-order semi-implicit backward-differentiation/Adams–Bashforth scheme.[54] Fourier–Chebyshev–Fourier spatial discretization is applied in all variables, and nonlinear terms are calculated with the collocation method. The numerical grid spacings in streamwise direction are $\delta_x^+=8.57$ for $L_x^+=360$, $\delta_x^+=10.91$ for $L_x^+=720$, and $\delta_x^+=15.15$ for $L_x^+=1000$ (see Table 1 for corresponding cases). Cases with higher $Wi$ along with longer $L_x^+$ have longer characteristic lengths and thus, can be resolved in larger grid sizes. The spanwise spacings are roughly kept constant in the range of $5.2 \le \delta_z^+ \le 5.8$ according to the number of Fourier modes adjusted for various $L_z^+$. In the wall-normal direction, 73 Chebyshev modes are used, giving $\delta_{y,\min}^+=0.081$ at the wall and $\delta_{y,\max}^+=3.7$ at the center of the channel. A constant time step size $\delta t=0.02$, which satisfies the Courant-Friedrichs-Lewy (CFL) stability condition, is adopted in Newtonian and lower $Wi$ cases ($Wi$ from 10 to 65). For higher $Wi$ cases ($Wi=75$, 85, and 90), where polymer stretches substantially, various time step sizes smaller than 0.02 are used to prevent the polymer stretching exceeding the maximum dumbbell length. To calculate the time step size, a simplified discretized version of the FENE-P constitutive equation is applied

$$\frac{\boldsymbol{\alpha}(t_2)-\boldsymbol{\alpha}(t_1)}{t_2-t_1}=f(\boldsymbol{\alpha}(t_1),\boldsymbol{v}(t_1)) \tag{5}$$

where $\boldsymbol{\alpha}(t)$ denotes the value of $\boldsymbol{\alpha}$ evaluated at time $t$ and $f$ denotes the value obtained from the terms evaluated at time $t$ in Eq. 3 excluding the time derivative. Here, the time step size $\Delta t=t_2-t_1$ is determined by satisfying the following inequality

$$\max_{\boldsymbol{x}}\ \mathrm{tr}\,(\boldsymbol{\alpha}(t_2)) < b \tag{6}$$

where $\boldsymbol{\alpha}(t_2)$ is calculated from Eq. 5 using the values at the previous time step $t_1$. If the $\Delta t$ obtained is smaller than 0.02, then it will be used as the current time step size. If not, then 0.02 will be the current time step size. This procedure is executed every once 50 time steps. It is simple as well as computationally trivial, while greatly improving the stability of the simulation.

**Table 1. Simulation Box Sizes $(L_x^+, L_z^+)$ and corresponding Bulk Reynolds Number $\mathrm{Re}_\mathrm{b} \equiv \rho U_\mathrm{b} l/(\eta_s+\eta_p)$, where $U_\mathrm{b}$ is the Bulk Velocity**

| Case | $L_x^+$ | $L_z^+$ | $Re_\mathrm{b}$ |
|---|---|---|---|
| Newtonian | 360 | 140 | 1164 |
| $Wi=10$ | 360 | 160 | 1160 |
| $Wi=15$ | 360 | 160 | 1187 |
| $Wi=20$ | 360 | 180 | 1243 |
| $Wi=25$ | 360 | 250 | 1315 |
| $Wi=35$ | 720 | 350 | 1481 |
| $Wi=55$ | 720 | 650 | 1588 |
| $Wi=65$ | 720 | 650 | 1628 |
| $Wi=75$ | 1000 | 700 | 1730 |
| $Wi=85$ | 1000 | 800 | 1725 |
| $Wi=90$ | 1000 | 700 | 1784 |

An artificial diffusivity term $1/(Sc\mathrm{Re})\nabla^2\boldsymbol{\alpha}$ with $Sc=0.5$ is added to the FENE-P equation to improve its numerical stability; this magnitude of artificial diffusivity is no larger than most other studies and should not affect the physical interpretation of the results.[8,9,12,23,37] The detailed numerical algorithm used in this study is documented in Xi.[13] The computer code used in this study is based on the Newtonian DNS code ChannelFlow written by Gibson.[55]

In the present work, we focus on flow in small domains. The idea is to approximately find the smallest simulation box size that still sustains the flow in which a long-lived turbulent states will exist. The process of simulation box minimization is stated as follows. First of all a threshold for the amount of time is set, that is, the simulation box has to sustain the turbulent motions longer than the threshold before the flow becomes laminar. The threshold should be at least longer than the viscous time scale $O(\mathrm{Re})$ to attain meaningful statistics. Here, 15,000 TUs ($\gtrsim$4Re) is chosen to be the threshold for the Newtonian and viscoelastic cases with $Wi < 75$. For higher $Wi$ ($Wi=75$, 85, and 90) cases, we find that the simulations are more prone to relaminarizing, so the threshold is reduced to 9000 TUs (=2.5Re). Next, we follow Xi and Graham's MFU studies to search for the box size for Newtonian and low-$Wi$ cases ($Wi \le 25$), as shown in Table 1. Details of the methodology can be found in Xi and Graham.[15] $L_x^+$ is first fixed at 360, and the overall trend is that as $Wi$ increases, larger $L_z^+$ is needed to sustain the turbulence. We further confirmed their report that no turbulence are found at higher $Wi$ using $L_x^+=360$. Therefore, the value for $L_x^+$ is increased to continue searching the box size for simulations at higher Weissenberg numbers. The same trend with increasing $Wi$ is observed for $L_z^+$. At simulations close to MDR ($Wi=75$, 85, and 90), an even longer as well as wider box is needed to attain sustained turbulence. These observations agree with previous findings that the correlation length scales in both streamwise and spanwise directions are increased with increasing viscoelasticity.[9] The final results for the approximate minimal box sizes at various $Wi$ are given in Table 1. All simulations reported here use these sizes.

## KL Decomposition and its Extension to Viscoelastic Flows

Consider a vector- or field-valued dataset $u=\{u_1, u_2, \ldots, u_{N_t}\}$ that has been obtained by sampling a process at $N_t$ equally spaced intervals $t_i, i=1,2,\ldots,N_t$, so $u_i=u(t_i)$. The sample mean is $\bar{u}=\frac{1}{N_t}\sum_{i=1}^{N_t} u_i$ and the fluctuation from the mean is $u'=\{u_1-\bar{u}, u_2-\bar{u}, \ldots, u_{N_t}-\bar{u}\}$. The inner product between two vectors $f$ and $g$ will be denoted $(f,g)$ and the corresponding norm $||f||=\sqrt{(f,f)}$.

The KL decomposition arises from solution of the following problem: given the set of samples $u'$, find a time-independent unit vector $\phi$ that maximizes $\overline{(u',\phi)}$. Solving this problem is facilitated by writing $\phi$ in the basis defined by the samples: $\phi=\sum_{i=1}^{N_t} c_i u'_i$. In the fluid dynamics literature, this approach is called the "method of snapshots."[33] The resulting Euler–Lagrange equation is the eigenvalue problem

$$Kc=\lambda c \tag{7}$$

where

$$K_{ij}=\frac{1}{N_t}(u'_i, u'_j) \tag{8}$$

This matrix is symmetric positive definite so its eigenvalues $\lambda_k$ are positive and the corresponding eigenvectors $c_k$ form an orthogonal basis for representing $u$: $\phi_k=\sum_{i=1}^{N_t} c_{ki}u'_i$. If we interpret $||f||^2=(f,f)$ as an energy, then $\frac{1}{N_t}\sum_{i=1}^{N_t}(u'_i, u'_i)=\mathrm{tr}\,K$ is the average energy contained in the fluctuations. Then, as $\mathrm{tr}\,K=\sum_{i=1}^{N_t}\lambda_i$, we see that the eigenvalues of $K$ determine the relative contribution of each eigenvector to the average energy.

In Newtonian fluid dynamics, the dataset of interest is the velocity field, so $u=\{\boldsymbol{v}(\boldsymbol{x},t_1), \boldsymbol{v}(\boldsymbol{x},t_2), \ldots, \boldsymbol{v}(\boldsymbol{x},t_{N_t})\}$, the relevant inner product is

$$(u_\alpha, u_\beta)=\frac{1}{V}\int_V \frac{1}{2}\rho\boldsymbol{v}(\boldsymbol{x},t_\alpha)\cdot\boldsymbol{v}(\boldsymbol{x},t_\beta)d\boldsymbol{x} \tag{9}$$

where $V$ is the volume of the domain, and the corresponding energy is the kinetic energy per unit volume

$$U_k=\frac{1}{V}\int_V \frac{1}{2}\rho\boldsymbol{v}\cdot\boldsymbol{v}d\boldsymbol{x} \tag{10}$$

Thus, the leading eigenvalues and eigenfunctions arising from the KL decomposition of a turbulent velocity field represent the velocity fields that capture the largest fraction of the fluctuating kinetic energy in the flow.

Extension to viscoelastic flow relies on the following observation. Consider a dilute solution of polymers modeled as bead-spring dumbbells[53] with Hookean springs. The number density of polymers is $n$, and the stress tensor for this model obeys the Oldroyd-B equation. Denoting the spring constant as $H$, the ensemble-averaged equilibrium end-to-end distance for the springs is $\sqrt{3kT/H}$ where $k$ is Boltzmann's constant and $T$ temperature. Now, we denote the end-to-end vector for a dumbbell, nondimensionalized with the length scale $\sqrt{kT/H}$, as $\boldsymbol{q}$. The ensemble-averaged elastic energy stored per dumbbell is then $\frac{1}{2}kT\langle\boldsymbol{q}\cdot\boldsymbol{q}\rangle=\frac{1}{2}kT\mathrm{tr}\,\langle\boldsymbol{qq}\rangle$.[53,56] (The total (free) energy per dumbbell also contains an entropic contribution[53] that does not concern us here.) Defining the conformation tensor $\boldsymbol{\alpha}=\langle\boldsymbol{qq}\rangle$, the total stored elastic energy in a volume $V$ of fluid is

$$U_e=\frac{1}{V}\int_V \frac{1}{2}G\ \mathrm{tr}\,\boldsymbol{\alpha}\ dV \tag{11}$$

where $G=nkT$ is the shear modulus of the fluid. Because $\boldsymbol{\alpha}$ is symmetric positive definite by construction, we can always decompose it as $\boldsymbol{\alpha}=\boldsymbol{b}\cdot\boldsymbol{b}$ where $\boldsymbol{b}$ is also symmetric.[57] We will call $\boldsymbol{b}$ the symmetric square-root (SSR) tensor. Now, observing that $\mathrm{tr}\,\boldsymbol{\alpha}=\mathrm{tr}\,\boldsymbol{b}\cdot\boldsymbol{b}=\boldsymbol{b}:\boldsymbol{b}$, we can write the elastic energy per unit volume as a quadratic form

$$U_e=\frac{1}{V}\int_V \frac{1}{2}G\ \boldsymbol{b}:\boldsymbol{b}\ dV \tag{12}$$

whose structure naturally motivates a generalized approach to KL decomposition of viscoelastic flows.

Returning now to the general KL formalism, we define a vector $u_\alpha=[\boldsymbol{v}_\alpha\,\boldsymbol{b}_\alpha]^T$ that contains both a velocity field $\boldsymbol{v}_\alpha$ and SSR field $\boldsymbol{b}_\alpha$ evaluated at time instant $t_\alpha$. Given also a vector $u_\beta=[\boldsymbol{v}_\beta\,\boldsymbol{b}_\beta]^T$, then we can define an inner product

$$(u_\alpha, u_\beta)_{ke}=\frac{1}{V}\int_V \frac{1}{2}\left(\rho\boldsymbol{v}_\alpha\cdot\boldsymbol{v}_\beta+G\boldsymbol{b}_\alpha:\boldsymbol{b}_\beta\right)dV \tag{13}$$

and a norm

$$||u||_{ke}^2=(u,u)_{ke} \tag{14}$$

In the Hookean dumbbell case, the quantity

$$||u||_{ke}^2=U_k+U_e \tag{15}$$

is precisely the mechanical energy per unit volume. For other models it is not, although the corresponding inner product still constitutes a useful formulation for KL decomposition. The traditional KL decomposition of a flow is recovered by replacing $G$ by zero in Eq. 13, and a KL decomposition that only addresses the stress distribution in the fluid emerges if $\rho$ is set to zero. We present results below from both the full mechanical energy-based decomposition and the elastic-energy-based decomposition.

In the present study, KL decomposition is applied to the entire dataset as well as the conditional datasets. The conditional datasets are the active dataset, which contains instantaneous flow fields that exhibit active turbulence features, and the hibernating dataset, containing flow fields exhibiting hibernating turbulence features. The idea of using conditional datasets is to investigate both the behaviors of active and hibernating turbulence, which also provides further insight into conventional unconditional study. Here, a cutoff value of the instantaneous log-law slope $A^*_{20-30}$, defined as the slope of the instantaneous velocity profile $U^*(y^*)$ vs. $y^*$ between $20\le y^*\le 30$, is used to partition the flow fields into hibernating ($A^*_{20-30}>A^*_{\mathrm{cutoff}}$) and active datasets. The sample means for the conditional KL decompositions are based on the conditional datasets instead of the entire datasets. The cutoff values are 5 for $Wi = 15$, 7 for $Wi=35$, 8 for $Wi=35$, and 9 for $Wi=75$ and 90. The cutoff value chosen varies regarding the Weissenberg numbers in order to properly reflect the hibernating/active statistics as well as to obtain enough samples in each conditional dataset. The number of samples for various datasets is shown in Table 2. Note that the numbers are affected by the statistics at different $Wi$. For example, at higher $Wi$ the number of samples collected in active datasets is much lower than the number in hibernating datasets because the flow is predominant in the hibernating state. Finally, all datasets can be enlarged by a factor of four by exploiting the reflectional symmetry across the $x$–$y$ midplane ($z=L_z/2$), as well as the rotational symmetry around the channel center line.[58] (Further enrichment by exploiting additional symmetries did not significantly change the results.)

## Results

### *Overview*

In this section, we present the overall results for the cases from Newtonian to MDR. Figure 3a shows the percentage of DR (DR%) at the corresponding $Wi$. Here, DR% $\equiv (C_{f,s}-C_f)/C_{f,s}\times 100\%$, where $C_f \equiv 2\tau_{\mathrm{w}}/(\rho U_{\mathrm{avg}}^2)$ is the friction factor of the viscoelastic flow and $C_{f,s}$ is the friction factor for the Newtonian flow. Here, $\tau_{\mathrm{w}}$ is the average wall shear stress and $U_{\mathrm{avg}}$ is the bulk fluid velocity. The error bars on the plot are the standard errors of the time-averaged quantity with the block-averaging method.[59] Here, we can see the various stages of viscoelastic turbulence: the onset of DR ($Wi \approx 10$), the monotonic increase of DR% with $Wi$, and the saturation of DR after $Wi=75$. Note that we denote the largest $Wi$ case, $Wi = 90$, as the MDR case hereinafter, as the curve reaches an asymptote close to 60% DR, where the percentage remains approximately invariant with $Wi$. The dashed line represents the level of DR% corresponding to the Virk MDR velocity profile.

Mean velocity profiles at various $Wi$ are shown in Figure 4. For comparison, the relation for viscous sublayer $U_m^+(y^+)=y^+$, the log-law layer for Newtonian turbulence ($U^+=2.5\ln(y^+)+5.5$) and Virk's asymptotic velocity profile for MDR ($U_m^+(y^+)=11.7\ln(y^+)-17.0$) are also presented. Although all the curves collapse in the viscous sublayer at $y^+ \leq 5$, differences appear in the buffer layer and the log-law layer. Note that even at this low Reynolds number, $\mathrm{Re}_\tau=84.85$, the Newtonian turbulence still closely follows the classical log-law relation away from the wall. As viscoelasticity is introduced and increased, the mean velocity profiles elevate and approach toward the Virk MDR profile. The curve of $Wi = 90$ displays a slight offset from the Virk MDR profile (i.e., a different intercept) but the same slope; this is a common observation in many studies at MDR (e.g., Ref. 5).

Table 2. Number of Samples used in Various Datasets

| Case | Unconditional | Active | Hibernating |
|---|---|---|---|
| Newtonian | 3804 | – | – |
| $Wi = 15$ | 3044 | 2404 | 912 |
| $Wi = 35$ | 2724 | 1188 | 1536 |
| $Wi = 55$ | 2404 | 652 | 2200 |
| $Wi = 75$ | 2320 | 476 | 2148 |
| $Wi = 90$ | 2384 | 416 | 2660 |

(a) DR%

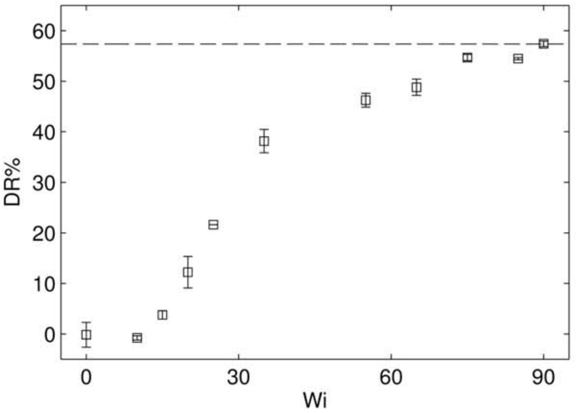

(b) Active and hibernating time scales

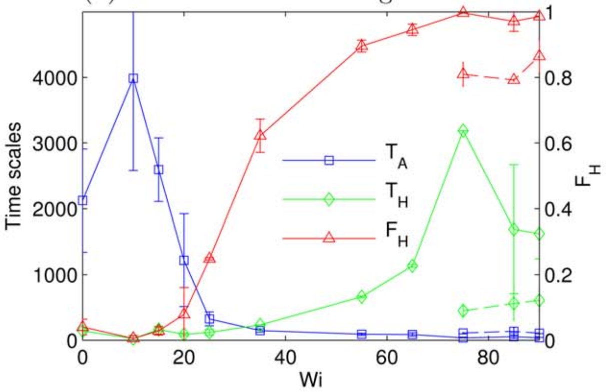

(c) Average energy

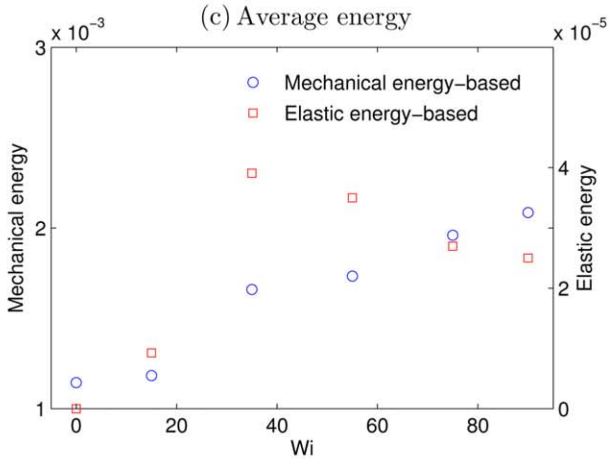

**Figure 3. (a) DR% for various *Wi*. The dashed line indicates the DR% asymptote reached at MDR. (b) Time scales (left *y*-axis) of average duration of active and hibernating intervals ($T_A$ and $T_H$), and the fraction of hibernation ($F_H$, right *y*-axis) as functions of *Wi* obtained from $A^*_{\mathrm{cutoff}}=7$. The dashed lines represent the results calculated from a new cutoff $A^*_{\mathrm{cutoff}}=9$. (c) Volume-averaged mechanical energy and elastic energy for various *Wi*.**

**[Color figure can be viewed in the online issue, which is available at wileyonlinelibrary.com.]**

### *Active and hibernating statistics*

*Transient Trajectories.* In this section, we first look at the time series of various quantities to provide a qualitative

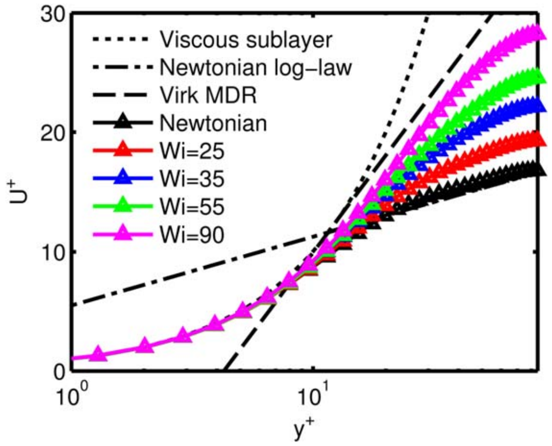

**Figure 4. Mean velocity profiles for different Weissenberg numbers.**

**[Color figure can be viewed in the online issue, which is available at wileyonlinelibrary.com.]**

view of how the intermittency between hibernating and active turbulence are changed by different levels of viscoelasticity. Figure 5 shows representative time trajectories for the Newtonian case and $Wi = 90$. From top to bottom, the quantities are bulk (volume-averaged) Reynolds shear stress, area-averaged wall shear rate, instantaneous log-law slope $A^*_{20-30}$, degree of bulk polymer stretching ($\mathrm{tr}\,\boldsymbol{\alpha}$) divided by the maximum dumbbell length $b$, and spatial-temporal shear rate patterns at the wall along the line $x = 0$. These are calculated from one arbitrarily chosen side of the channel, that is, volume averages are taken within half of the domain (from the wall to the center of the channel), and area averages are taken at the corresponding wall. In all cases, the average wall shear rate fluctuates around 2 due to the restriction of momentum balance. The time series of $A^*_{20-30}$ at various $Wi$ including intermediate $Wi$ can be found in Figure 6. Figure 5 shows that the Reynolds and wall shear stresses and polymer stretching are strongly anticorrelated with $A^*_{20-30}$, and thus, $A^*_{20-30}$ is sufficient to show the characteristics of the intermittency.[30]

During hibernation the flow displays properties like large magnitudes of $A^*_{20-30}$, which approach the Virk MDR log-law slope $A_{\mathrm{Virk}}$ of 11.7, low polymer stretching, and low Reynolds shear stress, compared to the active intervals. This hibernation phenomenon is Newtonian, as observed from the intervals between 1600–1800 and 3700–3900 TU in Figure 5a. A moderate degree of viscoelasticity causes the flow to enter hibernation more frequently but stay hibernating for approximately the same amount of time.[22,30] The change in hibernation frequency can be seen from the $A^*_{20-30}$ time series for $Wi{=}35$ (Figure 6), where $A^*_{20-30}$ approaches $A_{\mathrm{Virk}}$ much more often compared to Newtonian case and $Wi = 15$. Note that no discernible change in active and hibernating statistics is found for $Wi = 15$ as it is still below $Wi_c$.

At higher $Wi$, the results change substantially. From the $A^*_{20-30}$ time series for $Wi{=}55$, 75, and 90, it is seen that as $Wi$ increases, $A^*_{20-30}$ moves overall toward regions with higher values, which correspond to the states with lower drag. In particular, at MDR ($Wi{=}90$), $A^*_{20-30}$ travels intermittently around $A_{\mathrm{Virk}}$ and spends long time periods with $A^*_{20-30} > A_{\mathrm{Virk}}$. In addition to the overall shift to lower-drag states, the flow becomes much less chaotic as $Wi$ increases. This is seen from the smoother patterns in cases with high $Wi$, especially for MDR, where the sawtooth-like curves found in the Newtonian case no longer exist.

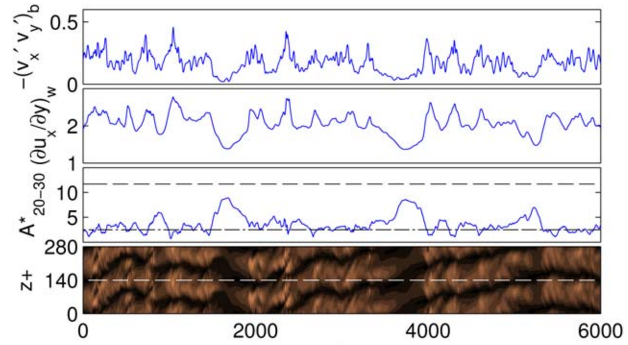

(a)Newtonian

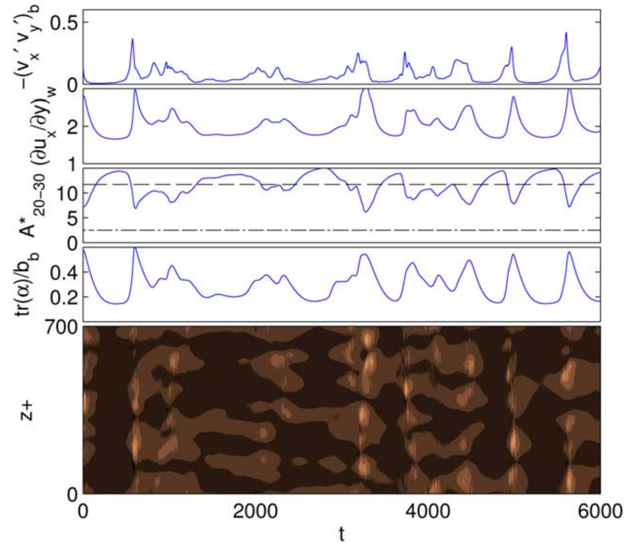

(b)MDR: Wi = 90

**Figure 5. Typical time series for Newtonian and MDR cases.**

**From top to bottom: bulk Reynolds shear stress, area-averaged wall shear rate, instantaneous log-law slope $A^*_{20-30}$ (dashed line: $A_{\mathrm{Virk}} = 11.7$; dashed-dot line: $A_{\mathrm{Newt}} = 2.5$), bulk polymer stretching ($\mathrm{tr}\,\alpha$ divided by the maximum dumbbell length $b$; not shown for Newtonian case), and spatial-temporal wall shear rate patterns along the line $x = 0$ (dark is low and bright is high; for clarity two periods in $z$ are shown in the Newtonian case). [Color figure can be viewed in the online issue, which is available at wileyonlinelibrary.com.]**

Now, we take a closer look at the spatiotemporal patterns for the Newtonian and MDR cases. The contour plots in Figure 5 show the wall shear rate as functions of $z$ and $t$ at a fixed streamwise location $x = 0$. To aid interpretation, two spatial periods in $z$ are plotted for the Newtonian case. The near-wall coherent structures are reflected by these patterns: the low-speed streaks correspond to the dark stripes composed of minima of the wall shear rate distributions in $z$ direction. We observe that in Newtonian case there is a continuous streak that drifts in the spanwise direction during the entire time domain. Whereas in MDR (only one period in $z$ is shown), multiple noncontinuous streaks are observed. These streaks are often cut by hibernation intervals and remain almost at the same spanwise position. Note that the flow is spanwise-variant even at the time instants where the shading seems uniform, that is, the difference is too small to

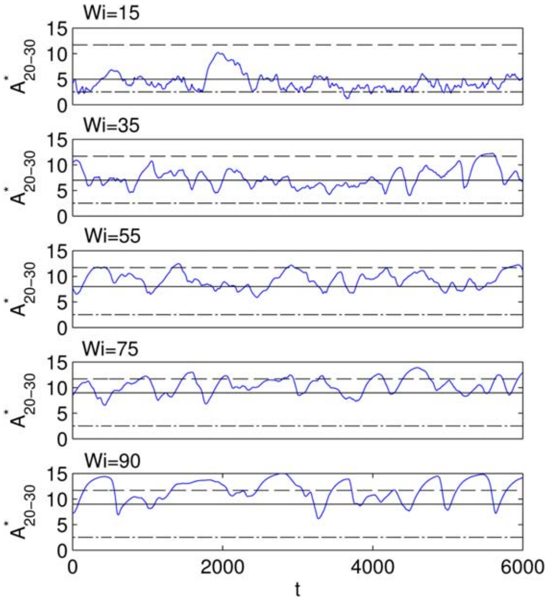

**Figure 6. Typical time series of instantaneous log-law slope $A^*_{20-30}$ at various Weissenberg numbers, from Newtonian to MDR.**

**Dashed lines: $A_{\mathrm{Virk}}=11.7$; dashed-dot lines: $A_{\mathrm{Newt}}=2.5$. Black solid lines: the cutoff values chosen for the conditional datasets in KL decomposition. [Color figure can be viewed in the online issue, which is available at wileyonlinelibrary.com.]**

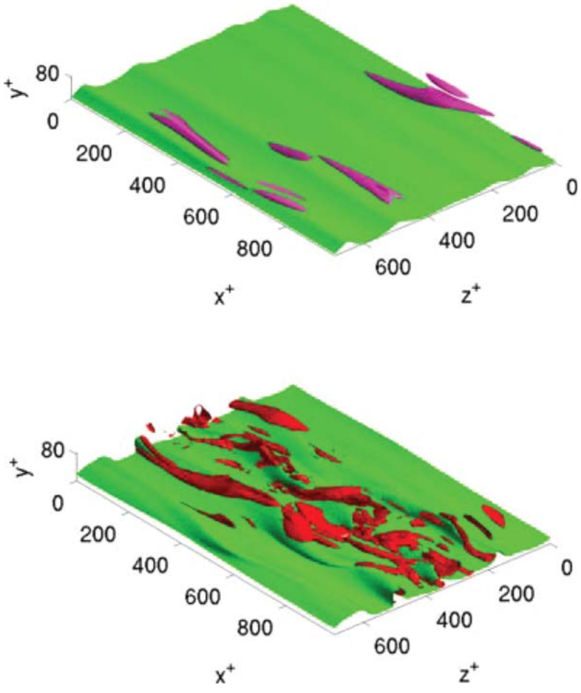

**Figure 7. Snapshots of hibernating (top) and active (bottom) turbulence at MDR ($Wi = 90$).**

**The green sheets are isosurfaces of the streamwise velocity $u_x=0.435$. The red patches are isosurfaces of the streamwise-vortex strength $Q_{2D}$ at the value of $8 \cdot 10^{-4}$ for the hibernating snapshot and $8 \cdot 10^{-3}$ for the active snapshot. [Color figure can be viewed in the online issue, which is available at wileyonlinelibrary.com.]**

be distinguished in the scale. This indicates the extremely weak vortex motions during hibernation in MDR.

To further investigate the instantaneous flow fields, we have selected two time instants that represent active and hibernating states, respectively, at MDR ($Wi = 90$), as circled in Figure 6. The flow fields are shown in Figure 7. The top and bottom plots show active and hibernating states, respectively. The green sheets with pleat-like structures are isosurfaces of the streamwise velocity $v_x=0.435$. The pleats correspond to low-speed streaks carrying slowly moving fluid away from the wall. Shown in red are isosurfaces of the streamwise-vortex strength $Q_{2D}$ (as defined in Ref. 15) at the value of $8 \cdot 10^{-4}$ for the hibernating snapshot and $8 \cdot 10^{-3}$ for the active one. In the active snapshot, we see wavy streaks with streamwise dependence, along with strong vortex motions near the streaks. The hibernating snapshot contains multiple nearly streamwise-invariant streaks with very weak vortex motions. Note that there would be no red isosurfaces at all on hibernating snapshot if $Q_{2D}=8 \cdot 10^{-3}$, the $Q_{2D}$ value for active snapshot, were used.

*Intermittency Quantification.* The intermittency of hibernating and active turbulence is quantified based on the approach in Ref. 30, as described below. First, a cutoff value $A^*_{\mathrm{cutoff}}=7$ is chosen to partition the instants into hibernating and active turbulence. If at a given instant $A^*_{20-30}$ is larger than $A^*_{\mathrm{cutoff}}$, it is identified as hibernating turbulence. Several quantities are calculated accordingly: the average duration of hibernating intervals $T_H$, the average duration of hibernating intervals $T_A$, and the fraction of hibernation $F_H$.

For $Wi \lesssim 25, T_H$ remains approximately constant with $Wi$, whereas $F_H$ becomes larger, whereas $T_A$ drops dramatically once $Wi \gtrsim 10$. As $Wi$ further increases, however, $T_H$ also eventually increases and finally, at MDR, $F_H$ saturates. Although $F_H$ levels off at MDR regime, the maximum in $T_H$ profile at $Wi=75$ appears to be a result of inadequate statistics. Looking back at the time series of $Wi = 90$ (Figure 5b), we find that the threshold 7 lies at the lower margin of the data for $A^*_{20-30}$, suggesting a high sensitivity of the statistics to the threshold. Thus, we chose another cutoff value of $A^*_{20-30}=9$ to reanalyze the high $Wi$ results. The three quantities $T_A, T_H$, and $F_H$ level off at MDR, confirming that the old cutoff value failed to quantify the intermittency in this regime.

To summarize, the time-series analysis presented above shows that the effect of viscoelasticity on minimal channel turbulence is twofold: first, it strongly suppresses the active turbulent dynamics that predominate in Newtonian flow and second, at sufficiently high Weissenberg number it stabilizes the dynamics of hibernating turbulence, allowing it to predominate in the MDR regime.

### KL analysis on viscoelastic turbulence

*Unconditional KL Analysis.* Now, we turn to a closer examination of the spatial structure of the flow. We first look at the results of KL decomposition based on unconditional datasets including both the velocity and SSR fields, that is, using the inner product defined by Eq. 13. Figure 8 shows the eigenvalue spectra at each $Wi$, sorted by descending order. The averaged mechanical energy per unit volume, $\mathrm{tr}\, K=\sum_{i=1}^{N_t} \lambda_i$, can be found in Figure 3c. These energies are nondimensionalized by outer units. Note that they reflect the fluctuations of the flow system. The kinetic energy and elastic energy of each mode are shown separately in the subplots. The cumulative energy percentage can also be found

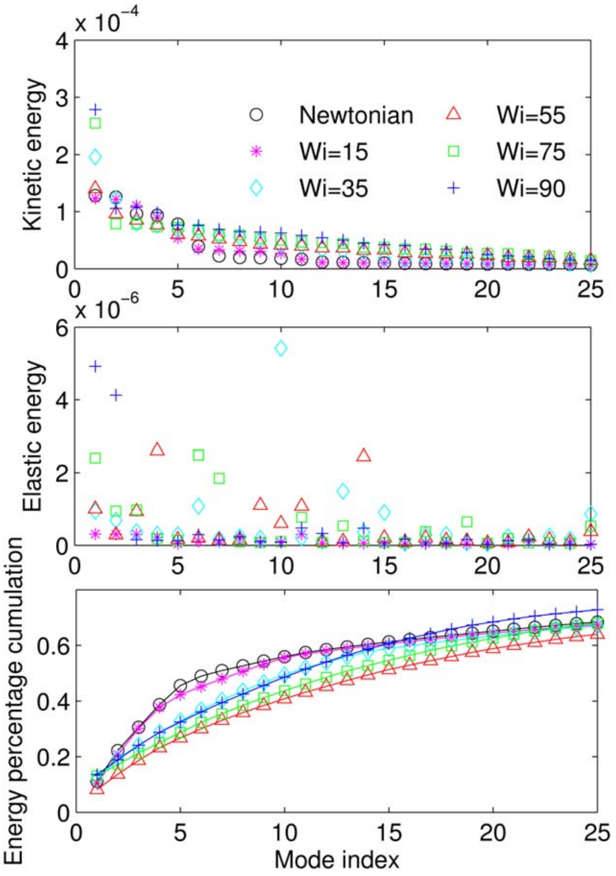

**Figure 8. Unconditional eigenvalue spectra from mechanical energy-based KL decomposition.**

All energies are nondimensionalized by outer units and based on unit volume. [Color figure can be viewed in the online issue, which is available at wileyonlinelibrary.com.]

later. It is shown that the order of magnitude of the kinetic energy is two orders higher than that of the elastic energy, leading to the consequence that the eigenmodes are virtually identical to those obtained from only velocity-based datasets. Nevertheless, the benefit of including SSR fields lies in the structural information of those corresponding energy-containing polymer stress fields. The mean velocity and polymer stretching profiles for different Wi are shown in Figure 9. As Wi increases, the velocity increases for a fixed pressure gradient; polymer stretches substantially at very high Wi.

Now, we examine the structures of the dominant eigenmodes. Figure 10a shows the most energetic mode $\phi_1$ for $Wi = 15$. This mode is streamwise invariant, and thus, contour plots of the streamwise velocity and polymer stretching fluctuations in the streamwise-normal channel cross section are presented. Hereinafter, streamwise-invariant modes will be shown in contour plots, whereas the modes with streamwise dependence will be presented via 3-D isosurface plots. Figure 10a is a typical roll mode that has been observed in both Newtonian and viscoelastic turbulence.[34,35] The top plot shows the streamwise velocity fluctuation. The dark and light shadings represent positive and negative values of fluctuations, respectively, whereas gray denotes zero fluctuation. Note that the magnitude of these eigenvectors is arbitrary, so the relative shadings, instead of the values themselves, are of importance.

The polymer conformation tensor field constructed by KL decomposition is shown in the lower plot. White denotes high magnitude of the $\boldsymbol{b}:\boldsymbol{b}$ fluctuation, whereas the black region indicates zero polymer stretching fluctuation. In the roll mode, the stretching fluctuations are focused at the region very close to the wall, with weaker maxima around the streamwise rolls. This agrees with previous findings that

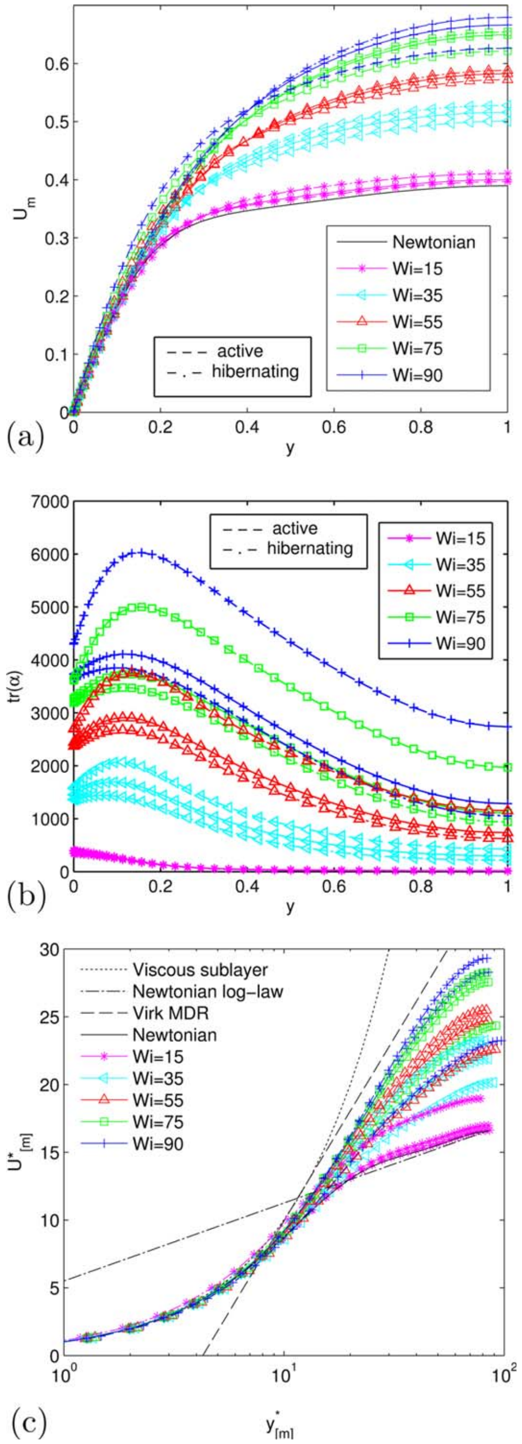

**Figure 9. (a) and (b) Mean velocity and mean polymer stretching profiles in outer units; (c) mean velocity profiles nondimensionalized by inner units based on conditionally averaged wall shear stress.**

[Color figure can be viewed in the online issue, which is available at wileyonlinelibrary.com.]

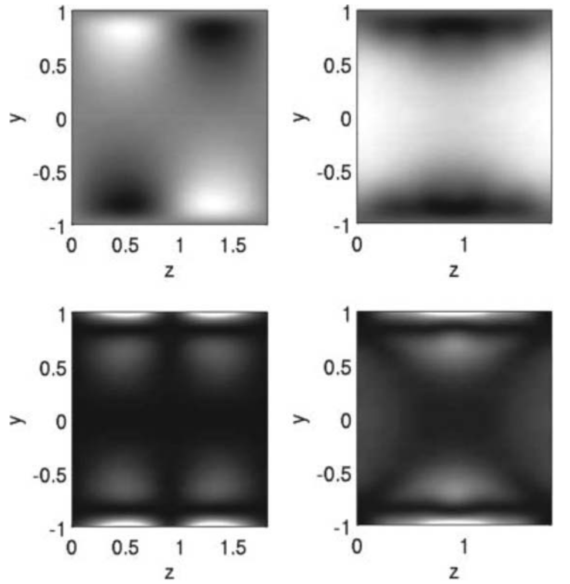

(a) (b)

**Figure 10. Contour plots of the streamwise velocity fluctuations (top) and polymer stretching (*b* : *b*) fluctuations (bottom) of the eigenmodes for *Wi* = 15.**

**(a) The most energetic mode $\phi_1$, a typical roll mode. (b) The fifth most energetic mode $\phi_5$, a typical sheet mode. Black and white denote negative and positive streamwise velocity fluctuations, respectively, while they represent zero and strong polymer stretching fluctuations, respectively.**

the polymers mainly act on the vortices to achieve DR.[46,48] However, the reason for the strongest polymer stretching fluctuation beneath the rolls is still unknown.

Figure 11 shows a most energetic propagating mode at $\mathrm{Wi}=15, \phi_{12}$. This mode contains streamwise dependence, and hence is shown in a 3-D isosurface plot with surfaces of streamwise velocity as well as polymer stretching fluctuations. The dark and light gray regions denote positive and negative streamwise velocity fluctuations, respectively, whereas the black regions denote polymer stretching fluctuations. Modes with this structure capture the streamwise variation of the quasistreamwise vortices.[34] Again, we see the polymer stretching fluctuations are primarily located around the vortices. The above results illustrate the capability of extracting relevant structures of polymer stress fields from the extended KL decomposition.

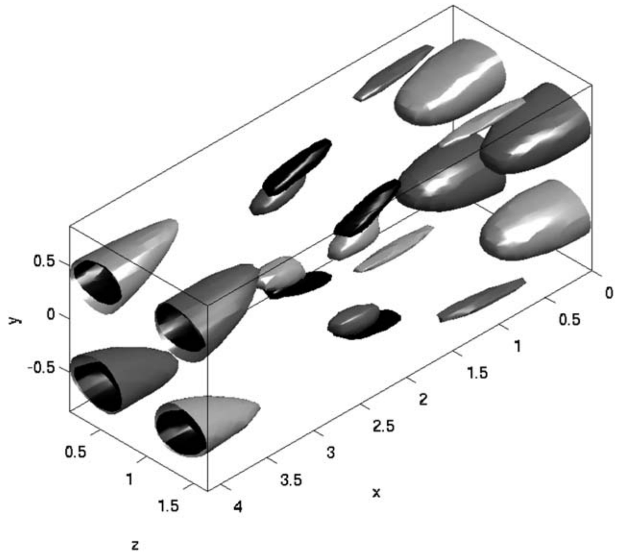

**Figure 11. Isosurface plot of the streamwise velocity fluctuations and polymer stretching fluctuations of $\phi_{12}$ at *Wi* = 15.**

**The dark and light gray surfaces denote positive and negative streamwise velocity fluctuations with the same absolute value, respectively. The black surfaces denote the polymer stretching fluctuations.**

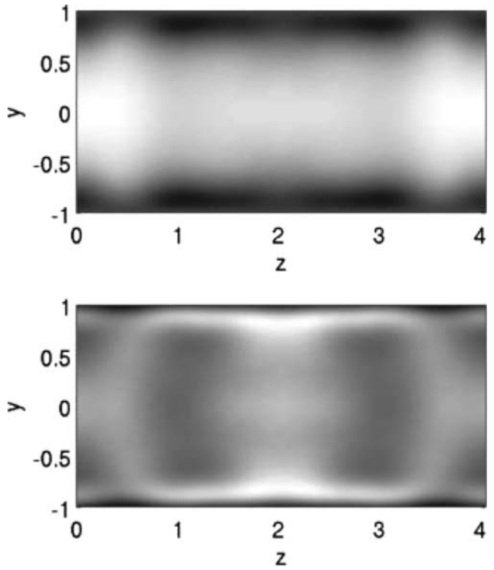

**Figure 12. The most energetic eigenmode $\phi_1$ for *Wi*=35, a typical sheet mode.**

**Contour plots of the streamwise velocity fluctuations (top) and polymer stretching fluctuations (bottom) are shown.**

It might be expected that at low *Wi* the dominant modes are almost identical to those found in Newtonian turbulence. However, we find that even at *Wi* = 15, there are dominant modes with a "sheet-like" structure, with very weak spanwise variation that are not present in Newtonian flow. (The name comes from 3-D plots in which isosurfaces of streamwise velocity or polymer stretch are nearly flat sheets.) An example, $\phi_5$ is shown in Figure 10b. These become more prominent as

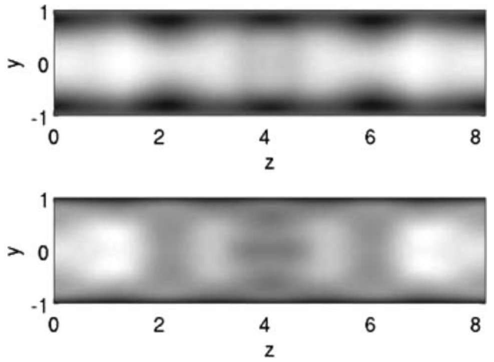

**Figure 13. The most energetic $\phi_1$ for *Wi* = 90, another sheet mode.**

**Contour plots of the streamwise velocity fluctuations (top) and polymer stretching fluctuations (bottom) are shown.**

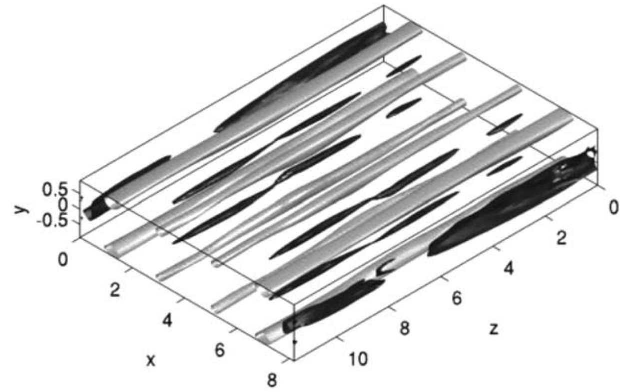

**Figure 14. Eigenmode $\phi_3$ for $Wi=75$ in the active dataset, an undefined mode.**

**Note that only the isosurfaces for streamwise velocity fluctuations are shown.**

$Wi$ increases; see Figures 12 and 13, for sheet modes at $Wi = 35$ and 90, respectively. These modes are streamwise invariant, and generally contain larger structures compared to roll modes and propagating modes. Their streamwise velocity fluctuation amplitudes vary predominantly in the wall-normal direction—they do not have a vortical structure. The corresponding polymer conformation fields contain localized structure with weak spanwise dependence. Moreover, strong polymer stretching fluctuations occur in different regions for sheet modes at different Weissenberg numbers. This observation will be further discussed later.

In addition to the roll, propagating, and sheet modes, there are modes that display nonsinuous structures in both streamwise and spanwise direction; an example is shown in Figure 14. In this eigenmode, there are several nonuniform size streamwise rolls (light surfaces), as well as some localized and nonsmooth patches (dark surfaces). Modes like this example are referred to as “undefined” modes hereinafter as they cannot be easily characterized.

Now, we summarize how the dominant eigenmodes are changed by viscoelasticity. Table 3 summarizes the structures of the five most energetic modes for different $Wi$. The first column in each entry represents unconditional datasets. The most important finding is the appearance of sheet modes in viscoelastic turbulence. These become the most energetic when $Wi \geq 35$. The polymer stretching fluctuations in these sheet modes are also modified by viscoelasticity. For low $Wi$ (Figure 10b), the fluctuation peaks at the wall region. As $Wi$ increases, the peak moves away from the wall, as seen in Figure 12. For MDR (Figure 13), the strongest fluctuation is located at the center. This is not observed in roll modes, where the fluctuations are located near the vortices for all $Wi$. Another important finding is that for higher $Wi$ cases, the propagating modes are no longer present among the leading modes, reflecting the dramatic weakening of the streamwise variation of the flow structures.

Now, we present the results from KL decomposition using only the SSR information, that is, the elastic energy. These eigenmodes capture the structures with high elastic energy fluctuations. The eigenvalue spectra are shown in Figure 15. The eigenmodes are expected to be very different from those in mechanical energy-based datasets, due to the predominance of kinetic energy over elastic energy in the flow system. Indeed, we observe that the most elastically energetic mode for all $Wi$ cases is a sheet mode, as seen in Figures 16a, 17a, and 18, for $Wi = 15$, 35, and 90, respectively. Unlike the sheet modes found in mechanical energy-based dataset, these SSR-based sheet modes consist of less localized structures, that is, structures with weaker spanwise dependence. Nevertheless, we observe the same trend of how viscoelasticity modifies the sheet modes. The peak of polymer stretching fluctuation moves from near the wall toward the center as $Wi$ increases. In addition to sheet modes, there are modes containing large structures that have substantial spanwise variation, as shown in Figures 19a, b. They are generally larger than those in mechanical energy-based dataset. The summary of the mode structure can be found in Table 4, where these large structure are denoted with an “L.” For unconditional datasets, we find that as $Wi$ increases sheet modes and L modes become dominant modes, replacing the roll modes, suggesting that the polymer stretching fluctuations are no longer confined at the near-wall region.

*Conditional KL Analysis.* In this section, we present the results for KL decomposition based on conditional datasets, where the fluctuating (primed) quantities are computed with respect to the conditional mean quantities. For reference, the means from unconditional, active, and hibernating datasets are all shown in Figure 9 as a reference. Figures 9a, b are the mean velocity and polymer stretching profiles, respectively, plotted against the distance from the wall in outer units. The unconditional averages, denoted by solid lines, show that both $U_m$ and $\mathrm{tr}\,(\boldsymbol{\alpha})_m$ increase monotonically with $Wi$. The active and hibernating averages are denoted by dashed lines and dashed-dot lines, respectively. Higher velocity and lower polymer stretching are observed in hibernating datasets, consistent with the features of hibernating turbulence observed previously.[30] We also find that a substantial difference between active and hibernating averages is found in $\mathrm{tr}\,(\boldsymbol{\alpha})_m$, but not in $U_m$. However, the difference in velocity profiles can be seen in the plot based on instantaneous inner units, as shown in Figure 9c.

A comparison of the modes constructed from mechanical energy-based KL decomposition of unconditional, active, and hibernating datasets is shown in Table 3. We see that there is little qualitative influence of conditioning on the energetic structures until $Wi \geq 35$. For $Wi = 15$ roll modes predominate and a sheet mode appears as the fifth mode in

**Table 3. Structure Categorization of the Five most Energetic Modes for Various Datasets from Mechanical Energy-Based KL Decomposition**

| Mode Index | $Wi = 15$ | $Wi = 35$ | $Wi = 55$ | $Wi = 75$ | $Wi = 90$ |
|---|---|---|---|---|---|
| 1 | R/R/R | S/R/S | S/R/S | S/R/S | S/U/S |
| 2 | R/R/R | R/R/R | U/R/R | R/R/R | S/R/S |
| 3 | R/R/R | R/R/R | R/R/U | U/R/U | R/U/R |
| 4 | R/R/R | R/R/R | S/R/S | R/U/R | R/S/R |
| 5 | S/S/S | R/R/R | R/U/R | R/R/R | R/R/R |

R: roll mode; S: sheet mode; U: undefined mode. The dataset is in the order of: unconditional/active/hibernating.

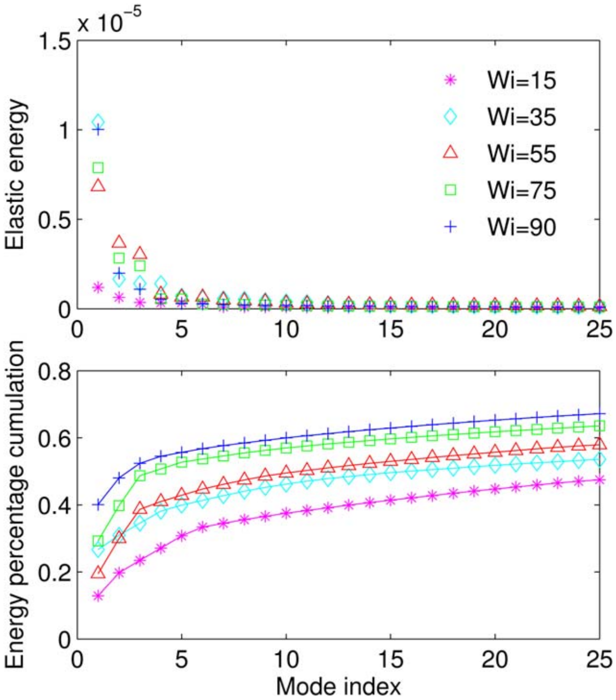

**Figure 15. Unconditional eigenvalue spectra from elastic energy-based KL decomposition.**

[Color figure can be viewed in the online issue, which is available at wileyonlinelibrary.com.]

all datasets. For cases with $Wi \geq 35$, the most energetic mode becomes a sheet mode in both unconditional and hibernating datasets, whereas it is a roll mode in all active datasets with only one exception of an undefined mode for $Wi = 90$. Moreover, roll modes dominate the active datasets for all $Wi$ except $Wi = 90$. For all $Wi$, the mode structures of unconditional and hibernating datasets are almost identical. For high $Wi$, this is expected because the hibernation period occupies most of the time. For low $Wi$, it might be that the hibernating turbulence is close to the Newtonian active states, and thus the vortex motions still dominate, which are reflected in existence of these energetic roll modes.

The conditional analysis is also conducted on the elastic energy-based KL decomposition, as summarized in Table 4. Again, it is observed that conditioning does not affect the energetic modes for $Wi = 15$, in which sheet and roll modes dominate. For $Wi \geq 35$, conditioning only rearranges the modes, that is, we still see sheet modes and modes with large structures predominate in all three kinds of dataset.

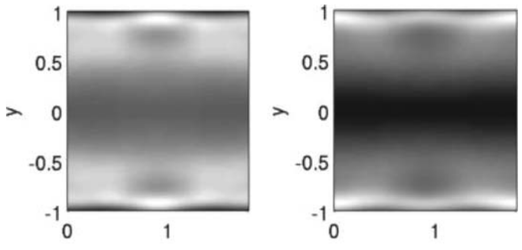

(a)$\phi_1$ (b)$\phi_2$

**Figure 16. The first two most energetic eigenmodes from elastic energy-based KL decomposition for *Wi* = 15.**

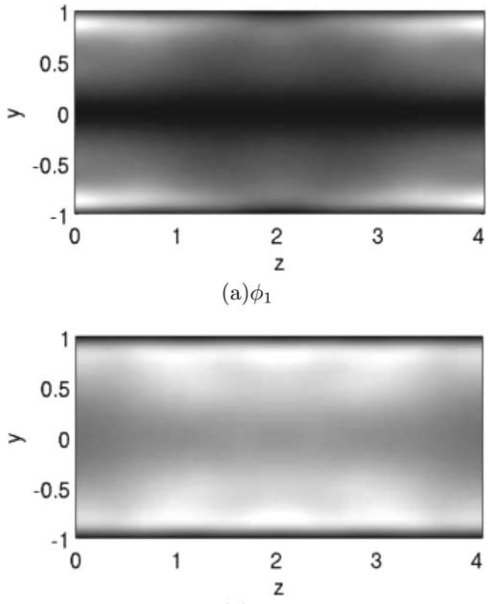

(a)$\phi_1$

(b)$\phi_2$

**Figure 17. The first two most energetic eigenmodes from elastic energy-based KL decomposition for *Wi*=35.**

## Discussion and Conclusions

In minimal channel flow at low $Re$ and $Wi$, the flow field intermittently cycles between states of active and hibernating turbulence. At low $Wi$, there is negligible DR and the durations $T_A$ and $T_H$ of the active and hibernating intervals are constant, with $T_A \gg T_H$. Once $Wi$ exceeds an onset threshold $Wi_{\text{onset}} \approx 10$, the drag begins to decrease and once a further threshold $Wi_c$ is exceeded, there is another regime where the fraction of time $F_H$ that the turbulence spends in the hibernating state increases: $T_A$ decreases dramatically, whereas $T_H$ remains approximately constant. The latter observation is consistent with the very weak turbulent structure found in the hibernation intervals; this structure is not effective at stretching polymers so in turn the polymers do not strongly affect flow during these intervals. These results were described in detail in Ref. 30. In the present work, we found that as $Wi$ further increases, $T_H$ also begins to increase, first gradually, and then fairly sharply once $Wi \gtrsim 60$, while the active intervals essentially vanish. At sufficiently high $Wi$, the mean velocity profile closely approaches the Virk MDR log-law result, and the instantaneous area-averaged velocity profile can transiently exceed the Virk profile. These observations indicate that the effect of viscoelasticity on minimal channel turbulence is twofold: first, it strongly suppresses the active turbulent dynamics that predominate in Newtonian flow and second, at sufficiently high $Wi$, it stabilizes the

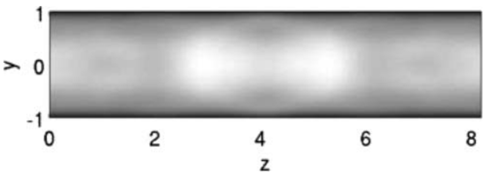

**Figure 18. The most energetic eigenmode $\phi_1$ from elastic energy-based KL decomposition for *Wi* = 90.**

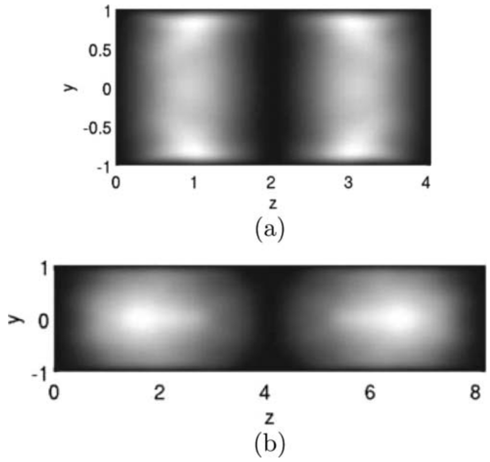

**Figure 19. The eigenmodes that contain large spanwise-periodic structures found in elastic energy-based KL decomposition.**

**(a) The third most energetic mode $\phi_3$ for $Wi=35$. (b) The second most energetic mode $\phi_2$ for $Wi=90$.**

dynamics of hibernating turbulence, allowing it to predominate in the MDR regime.

KL analysis of the velocity and stress fields reveals how these change as *Wi* increases. The most striking observation is that even at moderate *Wi*, a new family of eigenmodes becomes important, which have a sheet-like rather than a vortical structure. The stress-based KL analysis indicates that these structures become predominant at high *Wi*.

Recent work by Samanta et al.[5] may be closely connected to some of our observations. They performed simulations and experiments in the parameter regime where pipe flow has been observed to transition directly from laminar flow to MDR turbulence (cf. Ref. 1). The experiments were performed in pipe flow and the simulations in channel flow. In the simulation results, these authors also found a sheet-like flow structure at high *Wi*. These authors denoted the flow in this regime as "elasto-inertial turbulence" (EIT); based on our observations it seems likely that EIT is precisely the viscoelasticity-modified hibernating turbulence that we identified above.

As for hibernating turbulence itself, there is evidence that it is closely related to unstable nonlinear traveling wave solutions that have been found for the plane Couette and channel flow geometries. For example, Wang et al.[60] studied a class of traveling waves (TWs) in plane Couette flow that show very similar flow structures as hibernating turbulence. In particular, these TWs have streamwise dependence and Reynolds shear stress that asymptotically vanish as Re → ∞. It could also be that more than one class of TWs form this ultimate saddle structure. For example, the state-space structure that separates trajectories moving toward the two different basins of attraction, that is, laminar and turbulent flows, commonly referred to as the "edge structure," has a similar appearance as hibernation.[61–64] Recent work[29] shows that at least for channel flow at low Reynolds number, the edge state dynamics closely resemble MDR dynamics, and in particular display a Virk log-law slope for the mean velocity profile, even in the Newtonian limit. Figure 20 schematically illustrates the basic state-space structure of turbulent channel flow that seems to be emerging from these studies.

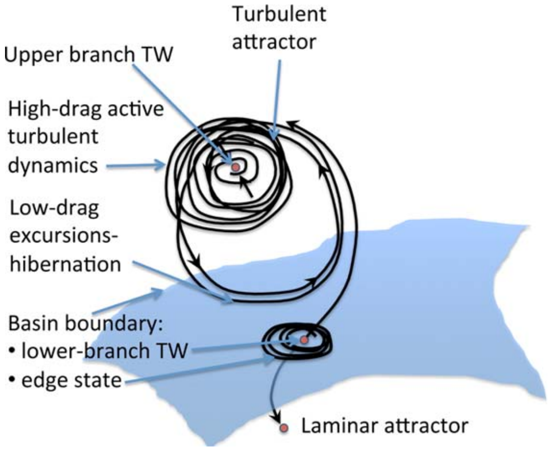

**Figure 20. Schematic state space structure of turbulent channel flow.**

**Upper branch and lower branch nonlinear traveling waves appear in pairs at saddle-node bifurcations close to the transition Reynolds number. If *Re* is not too large, the laminar state is linearly stable, implying the existence of a basin boundary between initial conditions that become turbulent and those that relax to laminar. "Edge states" are invariant solutions that lie on the basin boundary. [Color figure can be viewed in the online issue, which is available at wileyonlinelibrary.com.]**

The present work has focused on minimal channels, in which dynamics in the entire box are spatially correlated. In large domains, two changes arise.[65,66] First, larger scale structures can occur and second, spatiotemporal intermittency can arise, in which different parts of the domain are instantaneously displaying different behavior. The large scale structures have very weak velocity gradients and are thus not expected to interact substantially with the polymer dynamics. Spatiotemporal intermittency will certainly be a complicating factor, however, and is thus a necessary topic for future work.

**Table 4. Structure Characterization of the Five most Energetic Modes for Various Datasets from Elastic Energy-Based KL Decomposition**

| Mode Index | $Wi = 15$ | $Wi = 35$ | $Wi = 55$ | $Wi = 75$ | $Wi = 90$ |
|---|---|---|---|---|---|
| 1 | S/S/S | S/S/S | S/L/S | S/L/S | S/S/S |
| 2 | S/S/S | S/S/L | L/L/L | L/S/L | L/L/L |
| 3 | R/R/R | L/L/S | L/S/L | L/U/L | L/L/L |
| 4 | R/R/R | L/L/L | L/L/L | L/L/L | S/L/S |
| 5 | R/R/R | R/R/R | L/U/L | L/U/L | L/S/L |

R: roll mode; S: sheet mode; U: undefined mode; L: modes with large spanwise-periodic structure. The dataset is in the order of: unconditional/active/hibernating.

Finally, these observations do not directly address either the universality of MDR or how the polymer acts to prolong the lifetime of the hibernating turbulence intervals. We believe that the answer to the first question lies in the origin of hibernating turbulence as a Newtonian flow phenomenon and that the main impact of viscoelasticity is primarily to (1) unmask it by suppressing the predominant active turbulence structures and (2) to stabilize it at high $Wi$. The mechanism of this stabilization is as yet unknown.

## Acknowledgments

The authors are grateful to Charlie Doering, Becca Thomases, Michael Renardy, and Nusret Balci for interesting discussions. The viscoelastic DNS code used in this study is based on the Newtonian DNS code, *ChannelFlow*,[55] authored and maintained by John F. Gibson (Department of Mathematics and Statistics, University of New Hampshire); we are indebted to him for sharing that code and for his helpful advice. This work was supported by the National Science Foundation through grant CBET-1066223 and through support of MDG during his stay at the Institute for Mathematics and Its Applications, as well as the Air Force Office of Scientific Research through grant FA9550-11-1-0094 (Flow Interactions and Control Program).

The senior author's career has been greatly influenced by Bob Bird. As an undergraduate, he found BSL the most fascinating textbook he had ever read and this fascination has led to a scholarly career in transport and related topics. As a professor, he has been inspired by Bob's dedication to research, scholarship, the profession of Chemical Engineering and the University of Wisconsin-Madison. Hopefully, Bob will enjoy this small bit of doggerel in his honor:

You've probably heard
Of a fellow named Bird.
As a scholar he's greatly admired.
He loves to canoe
And speak languages too.
Generations of us he's inspired.

## Literature Cited

1. Virk PS. Drag reduction fundamentals. *AIChE J.* 1975;21(4):625–656.
2. Graham MD. Drag reduction in turbulent flow of polymer solutions. In: Binding DM, Walters K, editors. *Rheology Reviews 2004*. British Society of Rheology, Aberystwyth, UK, 2004:143–170.
3. White CM, Mungal MG. Mechanics and prediction of turbulent drag reduction with polymer additives. *Annu Rev Fluid Mech.* 2008;40: 235–256.
4. Virk PS. Elastic sublayer model for drag reduction by dilute solutions of linear macromolecules. *J Fluid Mech.* 1971;45:417–440.
5. Samanta D, Dubief Y, Holzner M, Schäfer C, Morozov AN, Wagner C, Hof B. Elasto-inertial turbulence. *Proc Natl Acad Sci USA.* 2013; 110(26):10557–10562.
6. Warholic MD, Massah H, Hanratty TJ. Influence of drag-reducing polymers on turbulence: effects of Reynolds number, concentration and mixing. *Exp Fluids.* 1999;27:461–472.
7. Min T, Choi H, Yoo JY. Maximum drag reduction in a turbulent channel flow by polymer additives. *J Fluid Mech.* 2003;492:91–100.
8. Ptasinski PK, Boersma BJ, Nieuwstadt FTM, Hulsen MA, van den Brule BHAA, Hunt JCR. Turbulent channel flow near maximum drag reduction: simulations, experiments and mechanisms. *J Fluid Mech.* 2003;490:251–291.
9. Li CF, Sureshkumar R, Khomami B. Influence of rheological parameters on polymer induced turbulent drag reduction. *J Non-Newtonian Fluid Mech.* 2006;140(1–3):23–40.
10. Warholic MD, Heist DK, Katcher M, Hanratty TJ. A study with particles image velocimetry of the influence of drag-reducing polymers on the structure of turbulence. *Exp Fluids.* 2001;31:474–483.
11. White CM, Somandepalli VSR, Mungal MG. The turbulence structure of drag-reduced boundary layer flow. *Exp Fluids.* 2004;36:62–69.
12. Housiadas KD, Beris AN, Handler RA. Viscoelastic effects on higher order statistics and on coherent structures in turbulent channel flow. *Phys Fluids.* 2005;17(3):035106.
13. Xi L. Nonlinear dynamics and instabilities of viscoelastic fluid flows. Ph.D. Thesis. University of Wisconsin-Madison, Madison, Wisconsin, USA, 2009.
14. Min T, Yoo JY, Choi H, Joseph DD. Drag reduction by polymer additives in a turbulent channel flow. *J Fluid Mech.* 2003;486:213–238.
15. Xi L, Graham MD. Turbulent drag reduction and multistage transitions in viscoelastic minimal flow units. *J Fluid Mech.* 2010;647: 421–452.
16. Sreenivasan KR, White CM. The onset of drag reduction by dilute polymer additives, and the maximum drag reduction asymptote. *J Fluid Mech.* 2000;409:149–164.
17. Benzi R, De Angelis E, L'vov VS, Procaccia I. Identification and calculation of the universal asymptote for drag reduction by polymers in wall bounded turbulence. *Phys Rev Lett.* 2005; 95:194502.
18. Procaccia I, L'vov VS, Benzi R. Colloquium: theory of drag reduction by polymers in wall-bounded turbulence. *Rev Mod Phys.* 2008; 80:225–247.
19. Yang SQ, Dou G. Drag reduction in a flat-plate boundary layer flow by polymer additives. *Phys Fluids.* 2005;17(6):065104.
20. Yang SQ, Dou GR. Modeling of viscoelastic turbulent flow in channel and pipe. *Phys Fluids.* 2008;20(6):065105.
21. Yang SQ, Dou G. Turbulent drag reduction with polymer additive in rough pipes. *J Fluid Mech.* 2009;642:279–294.
22. Xi L, Graham MD. Active and hibernating turbulence in minimal channel flow of Newtonian and polymeric fluids. *Phys Rev Lett.* 2010;104(21):218301.
23. Sureshkumar R, Beris AN. Direct numerical simulation of the turbulent channel flow of a polymer solution. *Phys Fluids.* 1997;9:743–755.
24. Housiadas KD, Beris AN. Polymer-induced drag reduction: effects of variations in elasticity and inertia in turbulent viscoelastic channel flow. *Phys Fluids.* 2003;15:2369–2384.
25. Dubief Y, White CM, Terrapon VE, Shaqfeh ESG, Moin P, Lele SK. On the coherent drag-reducing and turbulence-enhancing behaviour of polymers in wall flows. *J Fluid Mech.* 2004;514:271–280.
26. Jiménez J, Moin P. The minimal flow unit in near-wall turbulence. *J Fluid Mech.* 1991;225:213–240.
27. Hamilton JM, Kim J, Waleffe F. Regeneration mechanisms of near-wall turbulence structures. *J Fluid Mech.* 1995;287:317–348.
28. Jiménez J, Pinelli A. The autonomous cycle of near-wall turbulence. *J Fluid Mech.* 1999;389:335–359.
29. Xi L, Graham MD. Dynamics on the laminar-turbulent boundary and the origin of the maximum drag reduction asymptote. *Phys Rev Lett.* 2012;108(2):028301.
30. Xi L, Graham MD. Intermittent dynamics of turbulence hibernation in Newtonian and viscoelastic minimal channel flows. *J Fluid Mech.* 2012;693:433–472.
31. Lumley JL. *Stochastic Tools in Turbulence*. New York: American Press, 1970.
32. Holmes P, Lumley J, Berkooz G. *Turbulence, Coherent Structures, Dynamical Systems and Symmetry*. Cambridge University Press, Cambridge, UK, 1996.
33. Sirovich L. Turbulence and the dynamics of coherent structures, Part I. *Q Appl Math.* 1987;45:561–571.
34. Webber G, Handler R, Sirovich L. Karhunen-Loeve decomposition of minimal channel flow. *Phys Fluids.* 1997;9(4):1054–1066.
35. Angelis ED, Casciola C, L'vov V, Piva R, Procaccia I. Drag reduction by polymers in turbulent channel flows: energy redistribution between invariant empirical modes. *Phys Rev B.* 2003;67:056312.
36. Handler R, Housiadas K, Beris A. Karhunen-Loève representations of turbulent channel flows using the method of snapshots. *Int J Numer Methods Fluids.* 2006;52:1339–1360.
37. Kim K, Li CF, Sureshkumar R, Balachandar S, Adrian RJ. Effects of polymer stresses on eddy structures in drag-reduced turbulent channel flow. *J Fluid Mech.* 2007;584:281–299.
38. Samanta G, Oxberry GM, Beris AN, Handler RA, Housiadas KD. Time-evolution K-L analysis of coherent structures based on DNS of

turbulent Newtonian and viscoelastic flows. *J Turbulence*. 2008; 9(41):1–25.
39. Samanta G, Housiadas KD, Handler RA, Beris AN. Effects of viscoelasticity on the probability density functions in turbulent channel flow. *Phys Fluids*. 2009;21:115106.
40. Bhat S, Pal K, Chopra S. A study of intermittency and drag reduction in turbulence by dynamic laser light scattering. *Exp Fluids*. 2000;28(2):160–164.
41. de Angelis E, Casciola CM, Benzi R, Piva R. Homogeneous isotropic turbulence in dilute polymers. *J Fluid Mech*. 2005;531:1–10.
42. Perlekar P, Mitra D, Pandit R. Manifestations of drag reduction by polymer additives in decaying, homogeneous, isotropic turbulence. *Phys Rev Lett*. 2006;97:264501.
43. Cai WH, Li FC, Zhang HN. DNS study of decaying homogeneous isotropic turbulence with polymer additives. *J Fluid Mech*. 2010; 665:334–356.
44. Dubief Y, White CM, Shaqfeh ESG, Terrapon VE. Polymer maximum drag reduction: a unique transitional state. Annual Research Briefs. Center for Turbulence Research, Stanford University, 2011.
45. Stone PA, Waleffe W, Graham MD. Toward a structural understanding of turbulent drag reduction: nonlinear coherent states in viscoelastic shear flows. *Phys Rev Lett*. 2002;89:208301.
46. Stone PA, Roy A, Larson RG, Waleffe F, Graham MD. Polymer drag reduction in exact coherent structures of plane shear flow. *Phys Fluids*. 2004;16(9):3470.
47. Li W, Stone PA, Graham MD. Viscoelastic nonlinear travelling waves and drag reduction in plane Poiseuille flow. In: Mullin T, Kerswell RR, editors. *IUTAM Symposium on Laminar-Turbulent Transition and Finite Amplitude Solutions*. Dordrecht, The Netherlands: Springer-Verlag, 2005:289–312.
48. Li W, Xi L, Graham MD. Nonlinear travelling waves as a framework for understanding turbulent drag reduction. *J Fluid Mech*. 2006;565:353–362.
49. Li W, Graham MD. Polymer induced drag reduction in exact coherent structures of plane Poiseuille flow. *Phys Fluids*. 2007;19: 083101.
50. Kim K, Adrian RJ, Balachandar S, Sureshkumar R. Dynamics of hairpin vortices and polymer-induced turbulent drag reduction. *Phys Rev Lett*. 2008;100:134504.
51. Dimitropoulos C, Dubief Y, Shaqfeh E, Moin P, Lele S. Direct numerical simulation of polymer-induced drag reduction in turbulent boundary layer flow. *Phys Fluids*. 2005;17:011705.
52. Tamano S, Graham MD, Morinishi Y. Streamwise variation of turbulent dynamics in boundary layer flow of drag-reducing fluid. *J Fluid Mech*. 2011;686:352–377.
53. Bird RB, Curtiss CF, Armstrong RC, Hassager O. *Dynamics of Polymeric Liquids*, Vol. 2, 2nd ed. New York: Wiley-Interscience, 1987.
54. Peyret R. *Spectral Methods for Incompressible Viscous Flow*. New York: Springer-Verlag, 2002. ISBN 0-387-95221-7.
55. Gibson JF. Channelflow users' manual: release 0.9.18. 2009. Available at http://www.channelflow.org. Last accessed on January 17, 2014.
56. Casciola CM, de Angelis E. Energy transfer in turbulent polymer solutions. *J Fluid Mech*. 2007;581:419–436.
57. Balci N, Thomases B, Renardy M, Doering CR. Symmetric factorization of the conformation tensor in viscoelastic fluid models. *J Non-Newtonian Fluid Mech*. 2011;166(11):546–553.
58. Sirovich L. Turbulence and the dynamics of coherent structures, Part II. *Q Appl Math*. 1987;45:561–571.
59. Flyvbjerg H, Petersen HG. Error-estimates on averages of correlated data. *J Chem Phys*. 1989;91:461–466.
60. Wang J, Gibson JF, Waleffe F. Lower branch coherent states in shear flows: transition and control. *Phys Rev Lett*. 2007;98:204501.
61. Toh S, Itano T. A periodic-like solution in channel flow. *J Fluid Mech*. 2003;481:67–76.
62. Skufca JD, Yorke JA, Eckhardt B. Edge of chaos in a parallel shear flow. *Phys Rev Lett*. 2006;96:174101.
63. Schneider TM, Eckhardt B, Yorke JA. Turbulence transition and the edge of chaos in pipe flow. *Phys Rev Lett*. 2007;99:034502.
64. Duguet Y, Willis AP, Kerswell RR. Transition in pipe flow: the saddle structure on the boundary of turbulence. *J Fluid Mech*. 2008; 613:255–274.
65. Baltzer JR, Adrian RJ. Structure, scaling, and synthesis of proper orthogonal decomposition modes of inhomogeneous turbulence. *Phys Fluids*. 2011;23(1):015107.
66. Baltzer JR, Adrian RJ, Wu X. Structural organization of large and very large scales in turbulent pipe flow simulation. *J Fluid Mech*. 2013;720:236–279.

*Manuscript received Oct. 9, 2013, and revision received Dec. 12, 2013.*